

# SN 2020jgb

AUTHORS<sup>1</sup>

<sup>1</sup>*Center for Interdisciplinary Exploration and Research in Astrophysics (CIERA), Department of Physics and Astronomy, Northwestern University, 2145 Sheridan Road, Evanston, IL 60208, USA*

## ABSTRACT

*Keywords:* keywords

### 1. INTRODUCTION

- SN 2016jhr (Jiang et al. 2017) - thin shell, near- $M_{\text{Ch}}(1.38 M_{\odot}+0.01 M_{\odot})$
- SN 2016hmk as a double detonation (Jacobson-Galán et al. 2020) ( $0.85 M_{\odot}+0.02 M_{\odot}$ ) or a near-Chandrasekhar mass, 91bg-like object (Galbany et al. 2019)
- SN 2018byg ( $0.76 M_{\odot}+0.15 M_{\odot}$ ) (De et al. 2019)
- SN 2019ofm (De et al. 2020)

### 2. OBSERVATIONS

#### 2.1. Detection and Classification

SN 2020jgb was first discovered by the Zwicky Transient Facility (ZTF; Bellm et al. 2019; Graham et al. 2019) on 2020 May 03.463 UT (MJD 58972.463) with the 48-inch Samuel Oschin Telescope (P48) at Palomar Observatory. The internal designation is ZTF20aayhacx. It was detected at a magnitude of 19.86 in ZTF  $g$ -band, and J2000 coordinates  $\alpha = 17^{\text{h}}53^{\text{m}}12^{\text{s}}.651$ ,  $\delta = -00^{\circ}51'21''.81$ . The last non-detection was on 2020 April 27.477 (MJD 58966.477; 5.99 days before the first detection) up to a limiting magnitude of 20.7 in ZTF  $r$ -band.

#### Classification?

#### 2.2. Optical Photometry

We obtained  $gr$ -band photometry of SN 2020jgb with the ZTF camera. A Galactic extinction of  $E(B - V) = 0.404$  is reported by the maps of Schlafly & Finkbeiner (2011), for which we correct all our photometry using the extinction model proposed by Fitzpatrick (1999). We do not account for any additional host extinction due to the lack of any Na I D absorption in our spectra.

#### 2.3. Optical Spectroscopy

**Table 1.** Spectroscopic Observations of SN 2020jgb

$t_{\text{obs}}$	Phase	Telescope/	$R$	Range	Air
(MJD)	(d)	Instrument	( $\lambda/\Delta\lambda$ )	( $\text{\AA}$ )	Mass
58,976.42	−9.7	P60/SEDm	100	3770–9220	1.23
58,982.12	−4.2	NOT/ALFOSC	360	4000–9620	1.17
58,990.43	+3.9	P60/SEDm	100	3770–9220	1.23
58,997.44	+10.7	P60/SEDm	100	3770–9220	1.29
58,998.41	+11.6	Shane/Kast	1000?	3620–10720	1.28
59,008.41	+21.3	P60/SEDm	100	3770–9220	1.28
59,010.40	+23.3	P200/DBSP	700	3200–9500	1.27
59,023.58	+36.1	Keck I/LRIS	1100	3200–10250	2.04
59,107.29	+117.3	Keck I/LRIS	1100	3200–10250	1.31
59,143.26	+152.2	Keck I/LRIS	1100	3200–10250	2.16

NOTE—Phase is measured relative to  $t_{r,\text{peak}}$  in the host galaxy rest frame. The resolution  $R$  is reported for the central region of the spectrum.

We obtained optical spectroscopic follow-up of the object from  $\approx -10$  days to  $\approx +150$  days relative to the  $r$ -band peak, using the Spectral Energy Distribution Machine (SEDm; Blagorodnova et al. 2018) on the automated 60 inch telescope (P60; Cenko et al. 2006) at Palomar Observatory, the Kast Double Spectrograph (Miller & Stone 1994) at the Shane 3 m Telescope, the Andaluia Faint Object Spectrograph and Camera (ALFOSC)<sup>1</sup> installed at the Nordic Optical Telescope (NOT), the Double Beam Spectrograph (DBSP) on the 200 inch Hale telescope (P200; Oke & Gunn 1982), the Low Resolution Imaging Spectrograph (LRIS) on the Keck I telescope (Oke et al. 1995).

#### Data reduction?

#### 2.4. Near-infrared (NIR) Spectroscopy

<sup>1</sup> <https://www.not.iac.es/instruments/alfosc/>

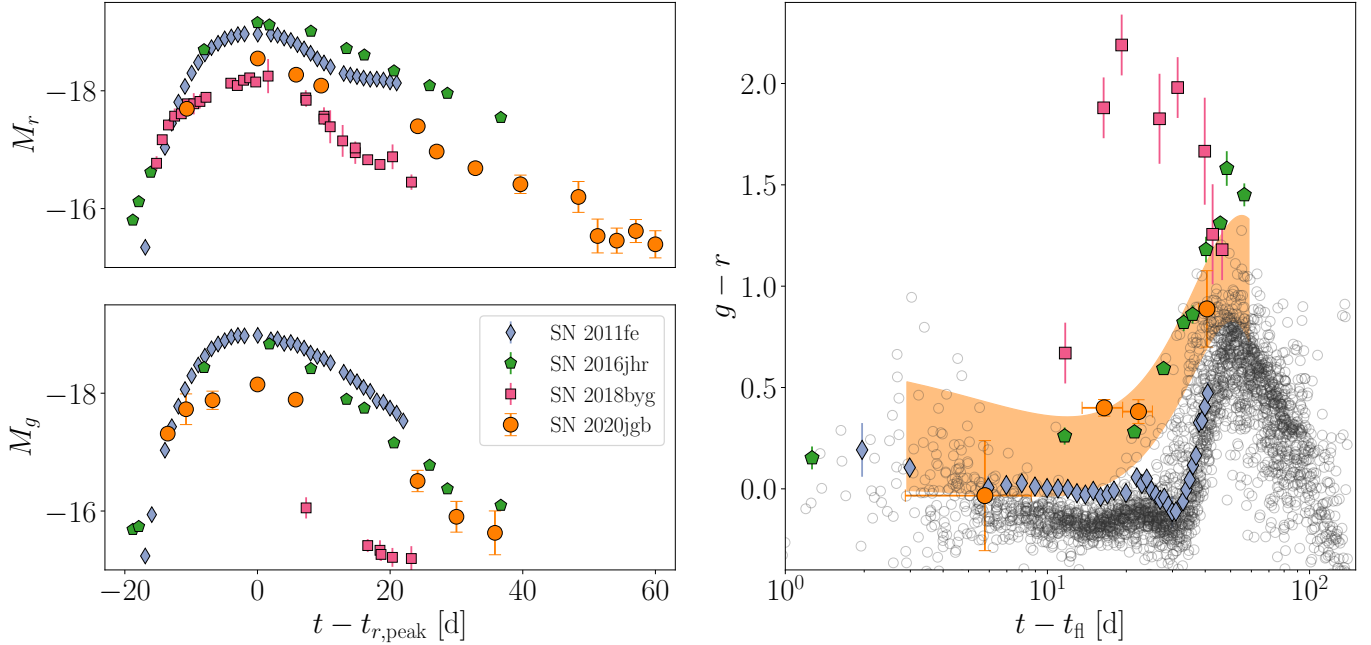


**Figure 1.** *Left:* comparison of the multi-color ( $g$  and  $r$  bands) light curves of SN 2020jgb to the normal SN Ia SN 2011fe and the He double detonation candidate SN 2018byg. *Right:* comparison of  $g - r$  color evolution to SN 2011fe and SN 2018byg, as well as 62 normal SNe Ia (open circles) with prompt observations within 5 days of first light by ZTF (Bulla et al. 2020). The shaded region denotes the  $1-\sigma$  credible interval of the color of SN 2020jgb until  $\sim 40$  days after the peak, estimated using Gaussian process.

We obtained one NIR ( $0.8\text{--}2.5\mu\text{m}$ ) spectrum of the transient using the Gemini near-infrared spectrometer (GNIRS; Elias et al. 1998) on the Gemini North telescope on 2020 June 9 ( $\sim 22$  days after  $r$ -band peak), for an integration time of 2400 s. The spectra were reduced with the `PypeIt` Python package (Prochaska et al. 2020; Prochaska et al. 2020).

### 3. ANALYSIS

#### 3.1. Photometric Properties

SN 2020jgb exhibited a fainter light curve than normal SNe Ia. In Figure 1, we compare the photometric properties of SN 2020jgb with the canonical SN Ia, SN 2011fe (Nugent et al. 2011) and two He-shell double detonation candidates, SN 2016jhr and SN 2018byg, with available photometric data on the Open Supernova Catalog (Guillochon et al. 2017).

The first detection was made on MJD=58972.46 in ZTF  $g$ -band. At a similar phase relative to the peak light, the luminosity was similar to the canonical object SN 2011fe and also the two double detonation candidates. But since then the light curve showed a slower rise than both SN 2011fe and SN 2016jhr, yet still faster than SN 2018byg. Near peak, the double detonation sample is heterogeneous in luminosity. The decline rate in  $g$ -band ( $\sim 0.07\text{ mag day}^{-1}$ ) of SN 2020jgb is similar as the canonical SNe Ia, SN 2011fe ( $\sim 0.06\text{ mag day}^{-1}$ ), and

is even slower than the normal-luminosity double detonation object, SN 2016jhr ( $\sim 0.09\text{ mag day}^{-1}$ ). Hence the decline rate is much slower than usual sub-luminous objects. SN 2018byg also exhibited an unusually slow decay in  $g$ -band ( $\sim 0.05\text{ mag day}^{-1}$ ), though the  $g$ -band peak was not covered.

In the right panel of Figure 1, we also compare the color evolution (ZTF  $g - r$ ) of these objects as measured from their first light  $t_{\text{fl}}$ , accompanied by 62 normal SNe Ia (open circles) observed within 5 days of  $t_{\text{fl}}$  by ZTF (from Bulla et al. 2020). For SN 2020jgb the early rise of the light curve was not well sampled, so we take the midpoint of the first detection and the last non-detection as an approximation of the explosion time, with the uncertainty ( $\approx 3$  days) being half of the offset between these two epochs. We also evaluate the  $1-\sigma$  uncertainty of the  $g - r$  color (the shaded region) in SN 2020jgb by fitting the light curve in each band with Gaussian process. All three double detonation candidates are undoubtedly redder than normal SNe Ia. At peak light, SN 2020jgb was not as red as the extreme case, SN 2018byg ( $g - r \approx 2.2$ ), but exhibited a similar color evolution as SN 2016jhr ( $g - r \approx 0.5$ ). Nonetheless, the colors eventually converged at  $\sim 50$  days after the first light, suggesting that the unusually red colors were not due to uncorrected dust extinction (De et al. 2019).

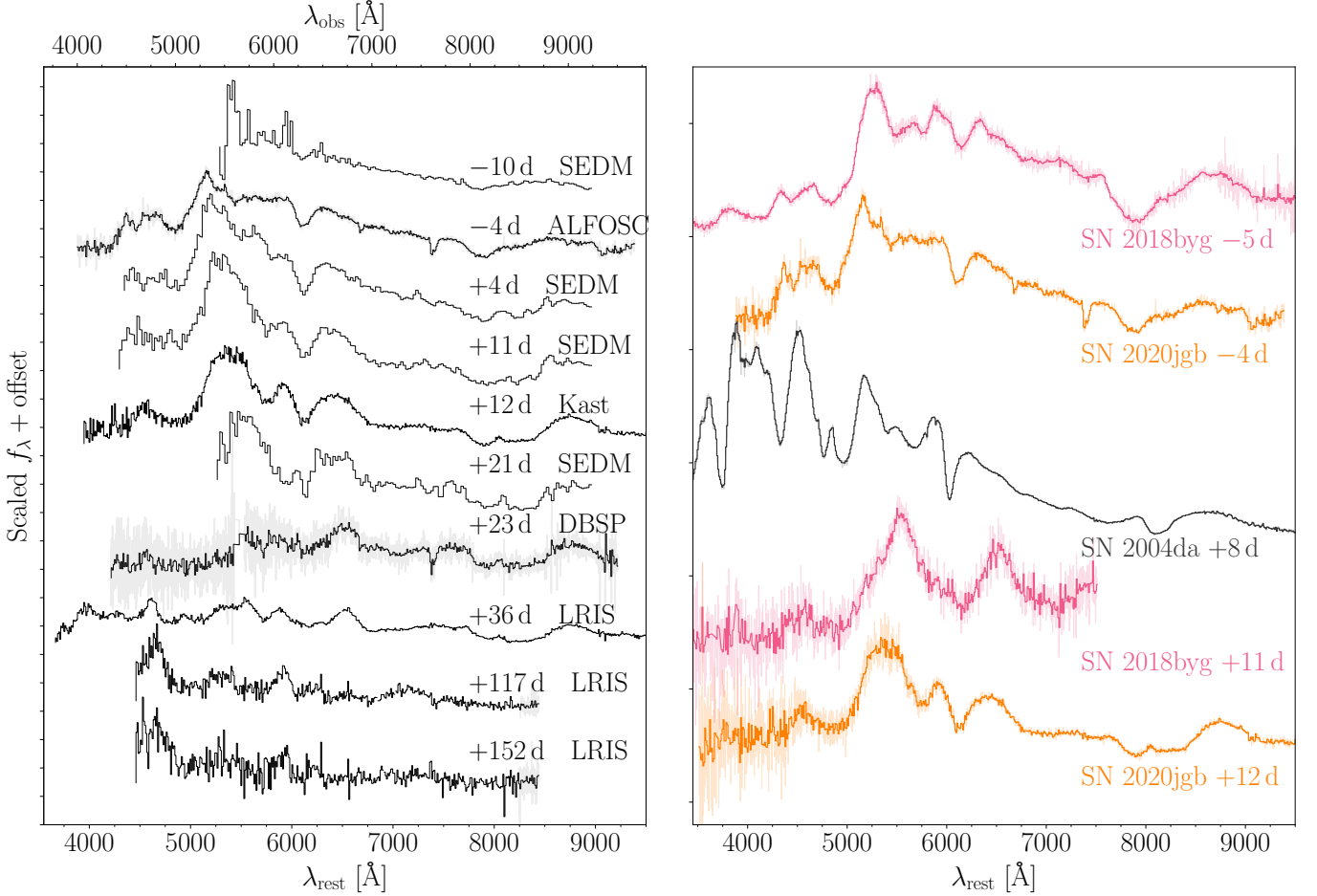


**Figure 2.** *Left:* optical spectroscopic sequence of SN 2020jgb. Rest frame phases (days) relative to the  $r$ -band peak and instruments used are posted next to each spectrum. The spectra are after Galactic extinction correction are shown in grey. The black lines are binned spectra with a bin size of  $10 \text{ \AA}$ , except for the SEDM spectra, whose resolution is lower than the bin size. In the last two spectra, we have subtracted the light from the host galaxy. *Right:* spectral comparison with SN 2018byg (sub-luminous He-shell double detonation) and SN 2004da (normal luminosity).

### 3.2. Optical Spectral properties

In Figure 2, we show the optical spectral sequence of SN 2020jgb, and compare its spectra with some other SNe Ia near peak luminosity. We did not perform the host galaxy subtraction except for the two nebular-phase spectra that were obtained over 100 days after the peak. The spectral sequence can thus be slightly blended with the light from the host. The earliest spectrum was obtained by SEDM  $\approx 10$  days before the  $r$ -band peak. The signal-to-noise ratio (SNR) is sufficiently high only at  $\gtrsim 5500 \text{ \AA}$ , where the continuum is almost featureless with some marginal detection of the Si II features at  $\approx 6100 \text{ \AA}$ , the trademark of SNe Ia. In subsequent spectra the Si II features become much more prominent and linger on until at least  $\sim 10$  days after the peak light. We fit the Si II feature with a Gaussian profile to get an expansion velocity of  $\approx 11,500 \text{ km s}^{-1}$  near peak light.

Also in the earliest spectrum, the wide absorption features by Ca II infrared triplet (IRT) have been visible at about  $7800\text{--}8200 \text{ \AA}$ . We fit the absorption features assuming each line in the triplet can be approximated by the same Gaussian profile (i.e., same amplitude and dispersion), and obtained a best-fit expansion velocity  $\gtrsim 26,000 \text{ km s}^{-1}$ . Such high-velocity features (HVF) remain visible for over 40 days. The photospheric velocity features (PVFs) at about  $8200\text{--}8600 \text{ \AA}$  is not visible until in our second spectrum  $\approx 4$  days before peak light. Since then we fit the broad absorption features with two different velocity components simultaneously. The velocity of HVFs slightly declines but stays above  $\approx 24,000 \text{ km s}^{-1}$ , and the velocity of PVFs declines from  $\approx 11,000 \text{ km s}^{-1}$  to  $\approx 9,000 \text{ km s}^{-1}$ . As in normal SNe Ia, the relative strength between HVFs and PVFs decreases with time.

The nebular phase spectra of SN 2020jgb are dominated by the Fe-group elements, showing some enhance-

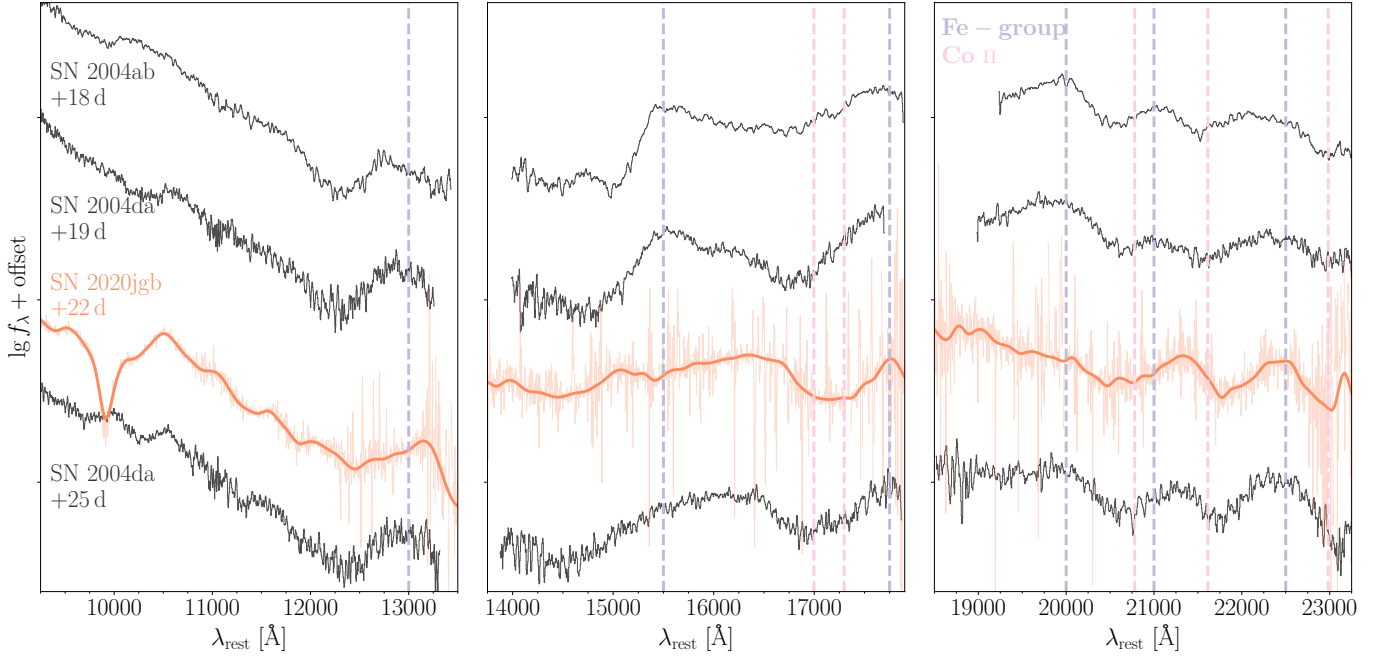


**Figure 3.** The NIR spectra of SN 2020jgb and two SNe Ia with normal maximum luminosity (SN 2004ab and SN 2004da, Marion et al. 2009), taken about three weeks after the peak. For each spectrum, the continuum at  $\gtrsim 1.2 \mu\text{m}$  is significantly reshaped by the Fe-group blanketing (emission features, blue vertical lines) and Co II absorption (pink vertical lines).

ment in flux between  $\approx 4500$  and  $\approx 6000 \text{ \AA}$ . We did not detect any emission feature related to  $[\text{Ca II}] \lambda\lambda 7291, 7324 \text{ \AA}$ , which is a hallmark for Calcium-rich gap transients and is also prominent in a few double detonation candidates (e.g., SN 2016hmk and SN 2019ofm; De et al. 2020).

SN 2020jgb highly resembles other double detonation candidates (e.g., SN 2018byg) in (i) the strong continuous absorption blueward of  $\approx 5000 \text{ \AA}$ , and (ii) the wide absorption feature of Ca II IRT, with the HVFs being prominent. In the double detonation scenario, a large amount of Fe-group elements will be synthesized in the outer regions of the ejecta, which will cause significant line-blanketing near peak light (Kromer et al. 2010; Polin et al. 2019), and also high velocity intermediate-mass elements like Ca II (Fink et al. 2010; Kromer et al. 2010). This makes SN 2020jgb another promising candidate for He-shell double detonation SN.

In §3.3 we will discuss the NIR spectra of the normal-luminosity object, SN 2004da, to which SN 2020jgb also show similarities (see Figure 3). Hence we also show one of the optical spectra of SN 2004da in Figure 2, which is typical for a normal SN Ia. It does not show any suppress of flux in  $g$ -band, and lacks the HVFs of Ca II IRT, in contrast to the sub-luminous double detonation objects.

### 3.3. NIR Spectral properties

In Figure 3, the NIR spectrum is presented along with three spectra in the sample of Marion et al. (2009) at similar phases. SN 2020jgb shows a strong absorption feature at  $\approx 0.99 \mu\text{m}$ , which is not seen in normal SNe Ia. This feature was still significant two weeks later, as detected by LRIS on Keck (see Figure 4), though it was only partially covered due to the limitation of bandwidth. In general, SN 2020jgb highly resembles normal SNe Ia in NIR band. The shape of the continuum redwards to  $\approx 1.2 \mu\text{m}$  is significantly altered by line-blanketing of Fe-group elements synthesized in the SN interior, as opposed to the Fe-group elements in the outermost region as ashes of shell helium burning. Just like normal SNe Ia, SN 2020jgb also show enhancement of flux at about  $1.3, 1.55, 2.0, 2.1$ , and  $2.25 \mu\text{m}$ , accompanied by several Co II absorption lines. It is especially similar to SN 2004da at +25 days after maximum as the steep increase in flux at  $\approx 1.55 \mu\text{m}$ , known as the  $H$ -band break, has become less prominent.

What is not seen in usual SNe Ia is the wide, deep absorption at  $\approx 0.99 \mu\text{m}$  (hereafter the  $1 \mu\text{m}$  feature), indicating its peculiarity. According to Marion et al. (2009), normal SNe Ia are nearly featureless in spectra around  $1 \mu\text{m}$  a few weeks past the week. There are several elements that may be associated with this feature. None of these identifications is fully satisfying, and usually other strong lines of the same elements are missing in the spectra. The nature of the  $1 \mu\text{m}$  feature remains un-

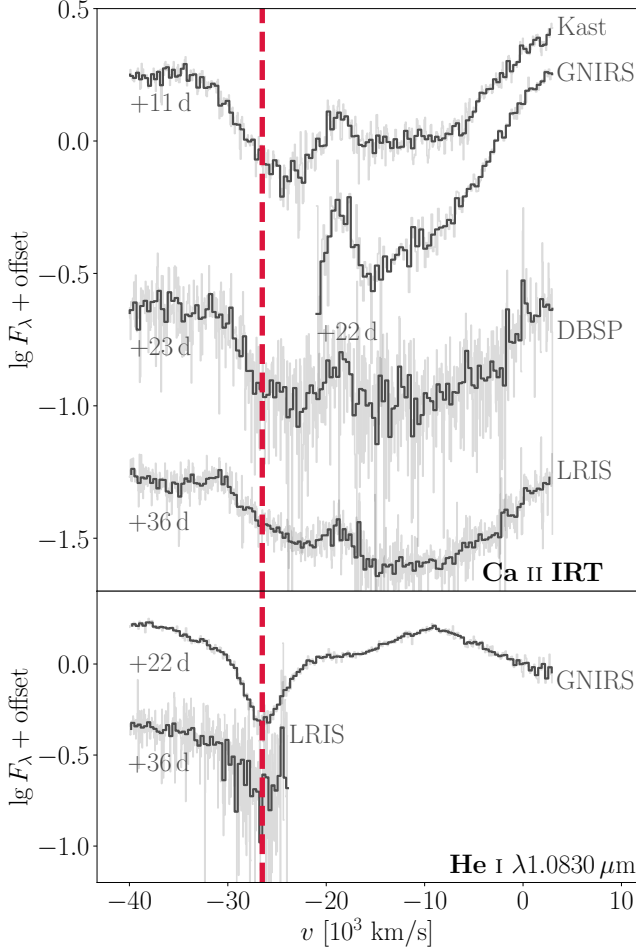


**Figure 4.** Spectra in the velocity space, comparing the high-velocity component of Ca II IRT and the absorption feature at  $\approx 0.99 \mu\text{m}$  assuming it is associated with He I at  $1.0830 \mu\text{m}$ .

certain. Chances are that this absorption is a mixture of multiple weaker lines.

The most attractive possibility is the strong He I line at  $1.0830 \mu\text{m}$ , as has predicted in sub-Chandrasekhar-mass He-shell double detonation models when considerable amount of helium in the shell is left unburnt (Boyle et al. 2017). Figure 4 shows that the  $1 \mu\text{m}$  feature, if associated with He I  $\lambda 1.0830 \mu\text{m}$ , has a high velocity ( $\approx 26,000 \text{ km s}^{-1}$ ), yet similar as the HVFs of Ca II IRT ( $\approx 24,000 \text{ km s}^{-1}$ ). The expansion velocity in the ejecta is roughly linearly proportional to the radius, so such a high velocity indicates that both the Ca II IRT and the tentative He I absorption line form far outside the normal photosphere, which has a velocity of only  $\approx 10,000 \text{ km s}^{-1}$ . In the sense, the He-shell double detonation scenario, in which the unburnt helium locates at the outermost ejecta, is indeed supported.

Still, this helium detection remains skeptical, since other He I are not unambiguously detected, such as

the He I  $\lambda 2.0581 \mu\text{m}$ . Considering a line velocity of  $\approx 26,000 \text{ km s}^{-1}$  and a host galaxy redshift of 0.0307, this line will be blueshifted to  $\approx 1.95 \mu\text{m}$  in the observer frame, so will be strongly blended by the strong telluric lines within  $1.8\text{--}2.0 \mu\text{m}$ . After telluric correction, the signal to noise ratio reaches  $\sim 5$ , with which we still cannot see any significant absorption feature. An upper limit of the equivalent width is determined to be  $< 2\%$  of the  $1.0830 \mu\text{m}$  line, while theoretically, the  $2.0581 \mu\text{m}$  line is supposed to be only a factor of 6–12 weaker, depending on temperature (Marion et al. 2009). Another fact is that the  $1 \mu\text{m}$  feature is as strong as the He I  $\lambda 1.0830 \mu\text{m}$  in many helium-rich core-collapse supernovae, say, Type Ib supernovae, in which the He I  $\lambda 2.0581 \mu\text{m}$  is weaker than the  $1.0830 \mu\text{m}$  line yet still prominent (Shahbandeh et al. 2022). If the  $1 \mu\text{m}$  feature is associated with He I, it would be very unusual if the  $2 \mu\text{m}$  feature is not seen at all, even if somehow blended by the telluric lines.

Other possibilities include the Mg II  $\lambda 1.0927 \mu\text{m}$ , the C I  $\lambda 1.0693 \mu\text{m}$ , and the Fe II  $\lambda 1.0500 \mu\text{m}$  &  $\lambda 1.0863 \mu\text{m}$ . The Mg II  $\lambda 1.0927 \mu\text{m}$  line is prevalent in the NIR spectra of SNe Ia, but usually disappears within a week after the peak luminosity (Marion et al. 2009), while the  $1 \mu\text{m}$  feature was still visible over a month after the peak in the Keck LRIS spectrum. The required radial velocity is  $\approx 30,000 \text{ km s}^{-1}$ ,  $\approx 20\%$  faster than the HVFs of Ca II IRT at the same phase. While such a high velocity for Mg II has never been seen in other SNe Ia, since high-velocity intermediate-mass elements like magnesium and calcium can be synthesized by the detonation of helium shell (Shen & Moore 2014), the Mg II origin of the  $1 \mu\text{m}$  feature cannot be strictly ruled out. But if we attribute this  $1 \mu\text{m}$  feature to high-velocity Mg II, we would expect an even stronger  $\lambda 0.9227 \mu\text{m}$  line to be blueshifted to the red edge of the Ca II IRT, which is not detected. Given the strength of the  $1 \mu\text{m}$  feature, the  $0.9227 \mu\text{m}$  line should not be completely obscured by the Ca II IRT features.

The C I  $\lambda 1.0693 \mu\text{m}$  line from the unburnt carbon is much less frequently seen than the Mg II  $\lambda 1.0927 \mu\text{m}$ . Hsiao et al. (2019) presented a sample of five SNe Ia with C I detections, showing the C I feature is strongest for those fainter, fast-declining objects. However, in their sample, the C I feature is a pre-maximum feature which fades away as the luminosity peaks, so the discrepancy in phase is large. The required expansion velocity  $\approx 22,000 \text{ km s}^{-1}$ , which is overwhelmingly faster than the estimated carbon velocity for the sample in Hsiao et al. (2019) ( $\sim 10,000\text{--}12,000 \text{ km s}^{-1}$ ), but still consistent with the HVFs of Ca II IRT. Nonetheless, no significant carbon absorption is detected in the optical band.



The Fe II features in SNe Ia usually start to develop roughly three weeks after the peak, which is about the same phase as we obtained our GNIRS spectrum. Two Fe II lines,  $\lambda 0.9998 \mu\text{m}$  and  $\lambda 1.0500 \mu\text{m}$ , are actually visible on the blue/red wings of the  $1 \mu\text{m}$  feature. The Fe II  $\lambda 1.0863 \mu\text{m}$  line is not yet seen in the GNIRS spectrum. They correspond to an expansion velocity of  $\approx 8,000 \text{ km s}^{-1}$ , which is consistent with the PVFs of the Ca II IRT at the same epoch. They also match the same two lines for normal SNe Ia (Marion et al. 2009), making the identification more reliable. Obviously, these two Fe II features are wider and shallower than the strong feature between them. We fit the  $1 \mu\text{m}$  feature with three Gaussian profiles. Two of them are set to be the blueshifted Fe II  $\lambda 0.9998 \mu\text{m}$  and  $\lambda 1.0500 \mu\text{m}$ , and the other is an uncorrelated Gaussian profile which mainly describes the absorption in the center. We find that the shallower and wider Fe II lines only make up  $\sim 40\%$  of the total equivalent width, and the rest  $\sim 60\%$  comes from the central feature, which cannot be accounted for by any Fe II feature at the same velocity. Given the similarity of the Fe-group line-blanketing between the GNIRS spectrum with the spectrum of SN 2004da at +25 days, the distribution of Fe-group elements inside each supernova ejecta should be somehow similar as normal SNe Ia, so the central region of the  $1 \mu\text{m}$  feature is not likely to be associated with Fe II either.

While the nature of the  $1 \mu\text{m}$  feature remains uncertain, other He-shell double detonation candidates also seem to show similar complexity in this region. In the currently small sample of five candidates, two objects (SN 2016jhr and SN 2019ofm) do not have any available NIR spectra, while the other three (at quite different phases though) all exhibit strong absorption features near  $1 \mu\text{m}$ , as shown in Figure 5. The  $1 \mu\text{m}$  feature for SN 2016hmk lies at a longer wavelength than SN 2020jgb, which corresponds to a lower expansion velocity, assuming they all have the same origin. The line velocity assuming a He I  $\lambda 1.0830 \mu\text{m}$  origin is  $\approx 21,000 \text{ km s}^{-1}$ , which, just like SN 2020jgb, is about the same as the HVFs of the Ca II IRT in the optical spectra. The PVFs of the Ca II IRT ( $\approx 10,000 \text{ km s}^{-1}$ ) is not significantly slower than that in SN 2020jgb. For SN 2018byg, the velocity of the  $1 \mu\text{m}$  feature with respect to the He I  $\lambda 1.0830 \mu\text{m}$  is still consistent with the HVFs of Ca II IRT. But given its exotic width and lower signal-to-noise ratio, the exact line velocity is hard to determine. It is highly likely to be a mixture of several different lines.

Unfortunately, the NIR spectra for both SN 2016hmk and SN 2018byg do not cover the  $2 \mu\text{m}$  region, thus it is not possible to identify the presence of helium decisively. But if the  $1 \mu\text{m}$  feature of these objects are

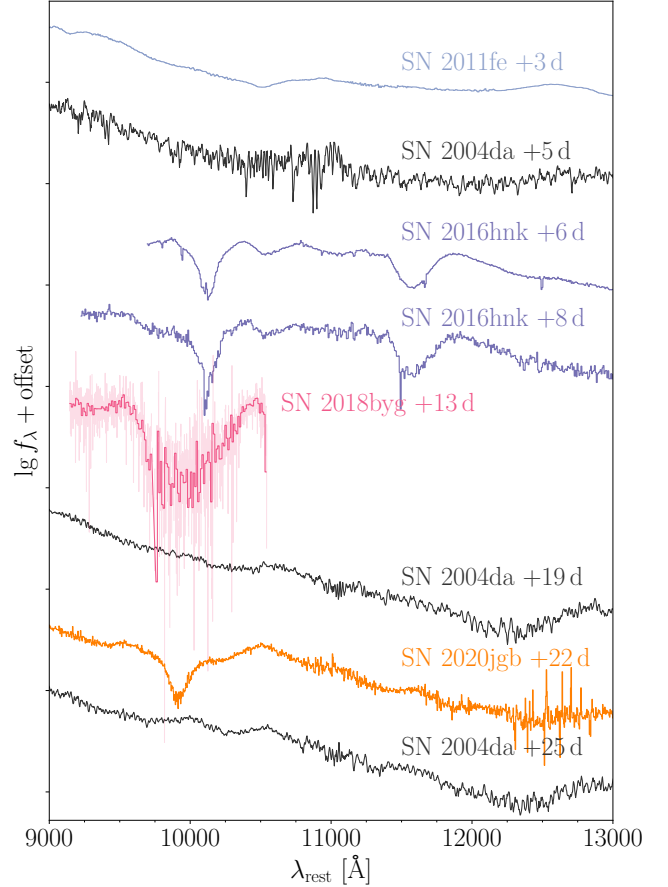


**Figure 5.** The NIR spectra (9,000 to 13,000 Å) of a few normal SNe Ia (SN 2011fe and SN 2004da) and three He-shell double detonation candidates, which are all subluminal SNe Ia (SN 2016hmk, SN 2018byg, and this source, SN 2020jgb). Spectra for SN 2004da were obtained from Marion et al. (2009), and other spectroscopic data were obtained from the WISEREP repository (Yaron & Gal-Yam 2012).

of the same origin, they are more likely to be correlated with the high velocity ejecta lying in the outmost region in the supernovae, because at least for SN 2020jgb and SN 2016hmk, the difference in their photospheric velocities cannot explain their discrepancy in the line velocities of the  $1 \mu\text{m}$  feature. Then helium is still a promising candidate to cause strong absorption near  $1 \mu\text{m}$  for these sub-luminous He-shell double detonation SNe Ia.

Alternatively, since the NIR spectra for the three objects were all obtained at different epochs, each  $1 \mu\text{m}$  feature can be of completely unrelated origin. This is to be confirmed in a more complete NIR spectral sequence in future He-shell double detonation SNe Ia. Even so, the seemingly ubiquitous  $1 \mu\text{m}$  feature in various phases is possibly a distinctive attribute against normal SNe Ia.

#### 4. HOST GALAXY

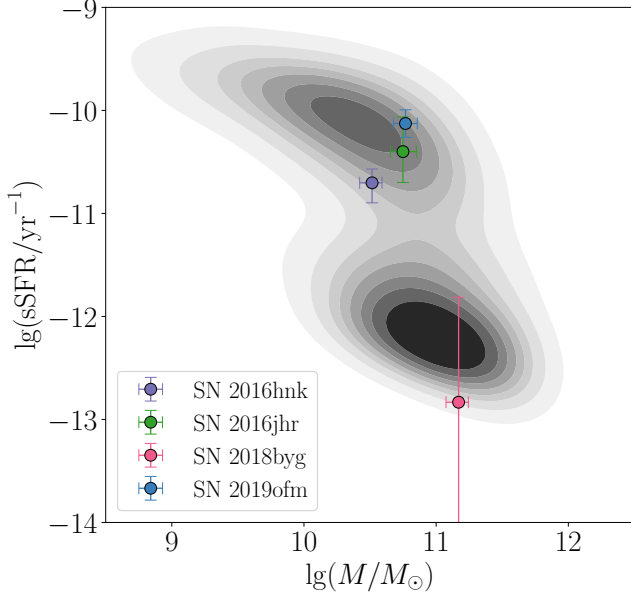


**Figure 6.** The specific star formation rate (sSFR) and the galactic mass for the host galaxies of He-shell double detonation candidates. The data for the host of SN 2016hmk are taken from Galbany et al. (2019), and for hosts we apply the galaxy parameters from the SDSS MPA-JHU DR8 catalog (Kauffmann et al. 2003; Brinchmann et al. 2004).

## 5. MODEL COMPARISONS

## 6. DISCUSSION AND CONCLUSION

## REFERENCES

- Bellm, E. C., Kulkarni, S. R., Graham, M. J., et al. 2019, *PASP*, 131, 018002, doi: [10.1088/1538-3873/aaecbe](https://doi.org/10.1088/1538-3873/aaecbe)
- Blagorodnova, N., Neill, J. D., Walters, R., et al. 2018, *PASP*, 130, 035003, doi: [10.1088/1538-3873/aaa53f](https://doi.org/10.1088/1538-3873/aaa53f)
- Boyle, A., Sim, S. A., Hachinger, S., & Kerzendorf, W. 2017, *A&A*, 599, A46, doi: [10.1051/0004-6361/201629712](https://doi.org/10.1051/0004-6361/201629712)
- Brinchmann, J., Charlot, S., White, S. D. M., et al. 2004, *MNRAS*, 351, 1151, doi: [10.1111/j.1365-2966.2004.07881.x](https://doi.org/10.1111/j.1365-2966.2004.07881.x)
- Bulla, M., Miller, A. A., Yao, Y., et al. 2020, *ApJ*, 902, 48, doi: [10.3847/1538-4357/abb13c](https://doi.org/10.3847/1538-4357/abb13c)
- Cenko, S. B., Fox, D. B., Moon, D.-S., et al. 2006, *PASP*, 118, 1396, doi: [10.1086/508366](https://doi.org/10.1086/508366)
- De, K., Kasliwal, M. M., Polin, A., et al. 2019, *The Astrophysical Journal*, 873, L18, doi: [10.3847/2041-8213/ab0aec](https://doi.org/10.3847/2041-8213/ab0aec)
- De, K., Kasliwal, M. M., Tzanidakis, A., et al. 2020, *The Astrophysical Journal*, 905, 58, doi: [10.3847/1538-4357/abb45c](https://doi.org/10.3847/1538-4357/abb45c)
- De, K., Kasliwal, M. M., Tzanidakis, A., et al. 2020, *ApJ*, 905, 58, doi: [10.3847/1538-4357/abb45c](https://doi.org/10.3847/1538-4357/abb45c)
- Elias, J. H., Vukobratovich, D., Andrew, J. R., et al. 1998, in *Society of Photo-Optical Instrumentation Engineers (SPIE) Conference Series*, Vol. 3354, *Infrared Astronomical Instrumentation*, ed. A. M. Fowler, 555–565, doi: [10.1117/12.317281](https://doi.org/10.1117/12.317281)
- Fink, M., Röpke, F. K., Hillebrandt, W., et al. 2010, *A&A*, 514, A53, doi: [10.1051/0004-6361/200913892](https://doi.org/10.1051/0004-6361/200913892)
- Fitzpatrick, E. L. 1999, *PASP*, 111, 63, doi: [10.1086/316293](https://doi.org/10.1086/316293)
- Galbany, L., Ashall, C., Höflich, P., et al. 2019, *Astronomy & Astrophysics*, 630, A76, doi: [10.1051/0004-6361/201935537](https://doi.org/10.1051/0004-6361/201935537)
- Graham, M. J., Kulkarni, S. R., Bellm, E. C., et al. 2019, *PASP*, 131, 078001, doi: [10.1088/1538-3873/ab006c](https://doi.org/10.1088/1538-3873/ab006c)
- Guillochon, J., Parrent, J., Kelley, L. Z., & Margutti, R. 2017, *ApJ*, 835, 64, doi: [10.3847/1538-4357/835/1/64](https://doi.org/10.3847/1538-4357/835/1/64)
- Hsiao, E. Y., Phillips, M. M., Marion, G. H., et al. 2019, *PASP*, 131, 014002, doi: [10.1088/1538-3873/aae961](https://doi.org/10.1088/1538-3873/aae961)
- Jacobson-Galán, W. V., Polin, A., Foley, R. J., et al. 2020, *The Astrophysical Journal*, 896, 165, doi: [10.3847/1538-4357/ab94b8](https://doi.org/10.3847/1538-4357/ab94b8)
- Jiang, J.-a., Doi, M., Maeda, K., et al. 2017, *Nature*, 550, 80, doi: [10.1038/nature23908](https://doi.org/10.1038/nature23908)

- Kauffmann, G., Heckman, T. M., White, S. D. M., et al. 2003, MNRAS, 341, 33, doi: [10.1046/j.1365-8711.2003.06291.x](https://doi.org/10.1046/j.1365-8711.2003.06291.x)
- Kromer, M., Sim, S. A., Fink, M., et al. 2010, ApJ, 719, 1067, doi: [10.1088/0004-637X/719/2/1067](https://doi.org/10.1088/0004-637X/719/2/1067)
- Marion, G. H., Höflich, P., Gerardy, C. L., et al. 2009, AJ, 138, 727, doi: [10.1088/0004-6256/138/3/727](https://doi.org/10.1088/0004-6256/138/3/727)
- Miller, J., & Stone, R. 1994, The Kast Double Spectograph, Lick Observatory technical reports (University of California Observatories/Lick Observatory).  
<https://books.google.com/books?id=QXk2AQAAIAAJ>
- Nugent, P. E., Sullivan, M., Cenko, S. B., et al. 2011, Nature, 480, 344, doi: [10.1038/nature10644](https://doi.org/10.1038/nature10644)
- Oke, J. B., & Gunn, J. E. 1982, PASP, 94, 586, doi: [10.1086/131027](https://doi.org/10.1086/131027)
- Oke, J. B., Cohen, J. G., Carr, M., et al. 1995, PASP, 107, 375, doi: [10.1086/133562](https://doi.org/10.1086/133562)
- Polin, A., Nugent, P., & Kasen, D. 2019, ApJ, 873, 84, doi: [10.3847/1538-4357/aafb6a](https://doi.org/10.3847/1538-4357/aafb6a)
- Prochaska, J. X., Hennawi, J. F., Westfall, K. B., et al. 2020, Journal of Open Source Software, 5, 2308, doi: [10.21105/joss.02308](https://doi.org/10.21105/joss.02308)
- Prochaska, J. X., Hennawi, J., Cooke, R., et al. 2020, pypeit/PypeIt: Release 1.0.0, v1.0.0, Zenodo, doi: [10.5281/zenodo.3743493](https://doi.org/10.5281/zenodo.3743493)
- Schlafly, E. F., & Finkbeiner, D. P. 2011, ApJ, 737, 103, doi: [10.1088/0004-637X/737/2/103](https://doi.org/10.1088/0004-637X/737/2/103)
- Shahbandeh, M., Hsiao, E. Y., Ashall, C., et al. 2022, ApJ, 925, 175, doi: [10.3847/1538-4357/ac4030](https://doi.org/10.3847/1538-4357/ac4030)
- Shen, K. J., & Moore, K. 2014, ApJ, 797, 46, doi: [10.1088/0004-637X/797/1/46](https://doi.org/10.1088/0004-637X/797/1/46)
- Yaron, O., & Gal-Yam, A. 2012, PASP, 124, 668, doi: [10.1086/666656](https://doi.org/10.1086/666656)